Juno sees the gas giant from new angles

First results from Juno show cyclones and massive magnetism on Jupiter

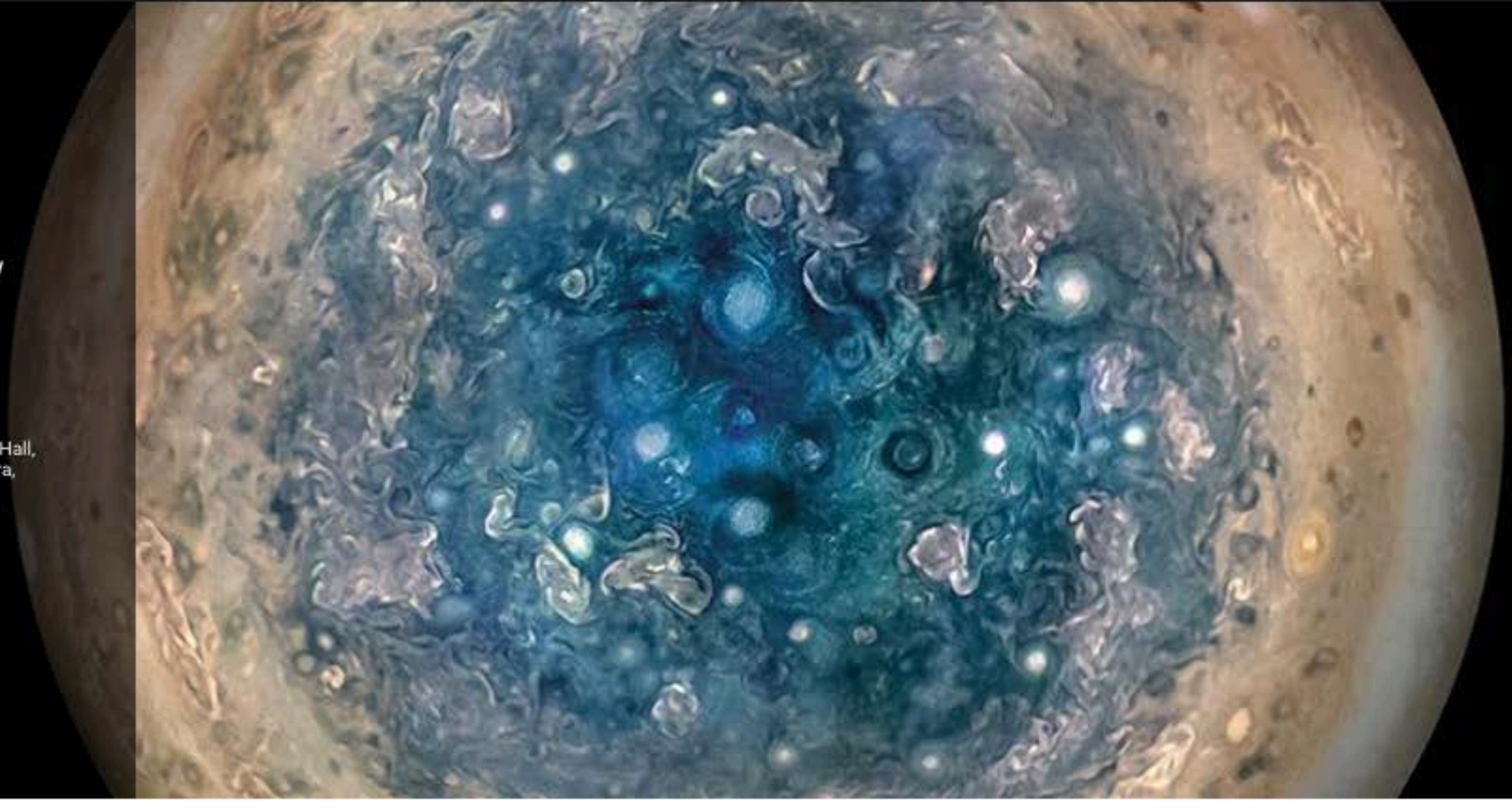

NASA/SwRI/MSSS/JPL-Caltech/Betsy Asher Hall, Gervasio Robles, Candy Hansen, Koji Kuramura, Eric De Jong, Scott BO

RESEARCH ARTICLE

GAS GIANT PLANETS

Jupiter's interior and deep atmosphere: The initial pole-to-pole passes with the Juno spacecraft

S. J. Bolton,[1]* A. Adriani,[2] V. Adumitroaie,[3] M. Allison,[4] J. Anderson,[1] S. Atreya,[5] J. Bloxham,[6] S. Brown,[3] J. E. P. Connerney,[7,8] E. DeJong,[3] W. Folkner,[3] D. Gautier,[9] D. Grassi,[2] S. Gulkis,[3] T. Guillot,[10] C. Hansen,[11] W. B. Hubbard,[12] L. Iess,[13] A. Ingersoll,[14] M. Janssen,[3] J. Jorgensen,[15] Y. Kaspi,[16] S. M. Levin,[3] C. Li,[14] J. Lunine,[17] Y. Miguel,[10] A. Mura,[2] G. Orton,[3] T. Owen,[18] M. Ravine,[19] E. Smith,[3] P. Steffes,[20] E. Stone,[14] D. Stevenson,[14] R. Thorne,[21] J. Waite,[1] D. Durante,[13] R. W. Ebert,[1] T. K. Greathouse,[1] V. Hue,[1] M. Parisi,[3] J. R. Szalay,[1] R. Wilson[22]

On 27 August 2016, the Juno spacecraft acquired science observations of Jupiter, passing less than 5000 kilometers above the equatorial cloud tops. Images of Jupiter's poles show a chaotic scene, unlike Saturn's poles. Microwave sounding reveals weather features at pressures deeper than 100 bars, dominated by an ammonia-rich, narrow low-latitude plume resembling a deeper, wider version of Earth's Hadley cell. Near-infrared mapping reveals the relative humidity within prominent downwelling regions. Juno's measured gravity field differs substantially from the last available estimate and is one order of magnitude more precise. This has implications for the distribution of heavy elements in the interior, including the existence and mass of Jupiter's core. The observed magnetic field exhibits smaller spatial variations than expected, indicative of a rich harmonic content.

The primary science goal of Juno is to improve our understanding of the origin and evolution of Jupiter, the history of the solar system, and planetary system formation in general. To constrain Jupiter's interior structure, Juno's onboard instruments probe below the cloud decks, gathering data about the planet's gravity, magnetic fields, and deep atmospheric composition. Juno's elliptical orbit provides multiple periapsis passes very close to Jupiter, within 1.06 Jupiter radii (R_J) of the jovigraphic equator, on its pole-to-pole trajectory. Measurements associated with a second science goal use Juno's unprecedented close-in polar orbits to explore Jupiter's polar magnetosphere and intense aurorae (*1*).

Juno's suite of science instruments includes X-band and Ka-band communications subsystems for determining Jupiter's gravity field, dual magnetometers to map Jupiter's high-order internal magnetic field, a six-channel microwave radiometer (MWR) operating at wavelengths between 1 and 50 cm to probe Jupiter's deep atmosphere, and a color camera (JunoCam) and an infrared spectrometer and imager (JIRAM) to capture views of Jupiter. Juno also carries a suite of field and particle instruments for in situ sampling of Jupiter's magnetosphere and investigation of its powerful aurora (*1*).

The poles of Jupiter

The JunoCam instrument is a visible-light camera with blue, green, red, and methane (centered at 890 nm) filters (*2*). Figure 1 shows close-up three-color images of the north and south poles of Jupiter obtained 27 August 2016, resolving details as small as 50 km. The wealth of detail in these images surpasses that of previous spacecraft because their trajectories were close to Jupiter's equatorial plane, whereas Juno's orbits were closer to the planet and oriented over the poles. Only Pioneer 11 had acquired nonoblique images over Jupiter's north pole, but at 10 times the distance of Juno (*3*).

Within 30° planetocentric latitude from each pole, the predominant zonal banded structure of lower latitudes breaks down. This boundary is coincident with a local drop in the zonal winds (*4*, *5*). Within these polar regions, the banded structure is replaced by discrete features that are embedded in a background that is darker than anything at lower latitudes. The brightest features are ovals with external spiral-like extensions. A time-lapse sequence of the images reveals that the ovals are cyclones; they exhibit counterclockwise motion in the northern hemisphere. On this initial perijove pass, northern ovals cover a range of diameters from ~1400 km down to JunoCam's 50-km resolution limit. In the south, they range from 200 to 1000 km, and most lie between 71° and 74°S (all latitudes are planetocentric). In both hemispheres, some cyclones appear clustered near the poles. The other bright regions in both hemispheres are amorphous; they resemble much smaller chaotic features at lower latitudes first detected in Voyager images (*6*). In the north, the largest of these is on the order of 4000 to 7000 km in size. In the south, several are concentrated between 68° and 73°S and stretch over 25° of longitude (10,000 km).

Jupiter's poles appear to be different from Saturn's in two specific ways. First, there is no equivalent to Saturn's north polar hexagon (*7*), although circumpolar waves are observed (*8*). Second is the lack of a vortex that is fast (150 m s^{-1}), compact (2° or 2500 km in radius), and centered on the pole, like those at the north or south poles of Saturn (*9*, *10*). Although the area within about 3° of latitude around the north pole is unilluminated, the south pole is visible and the features visible there are similar to others in the region. Thus, the polar dynamics and structures of the atmospheres of these two planets are fundamentally different. Future observations will better establish the full morphology of the poles at all longitudes and characterize their evolution in time.

An unusual high-altitude cloud is visible past Jupiter's terminator near the top portion of the north polar image in Fig. 1. It is a roughly circular feature with a diameter on the order of 7000 km. The effect of shadowing in Jupiter's clouds is evident. This cloud feature must be several scale heights (57 ± 21 km) above Jupiter's main polar

[1]Southwest Research Institute, San Antonio, TX 78238, USA. [2]Institute for Space Astrophysics and Planetology, National Institute for Astrophysics, 00133 Rome, Italy. [3]Jet Propulsion Laboratory/Caltech, Pasadena, CA 91109, USA. [4]Goddard Institute for Space Studies, New York, NY 10025, USA. [5]University of Michigan, Ann Arbor, MI 48109, USA. [6]Harvard University, Cambridge, MA 02138, USA. [7]Space Research Corporation, Annapolis, MD 21403, USA. [8]NASA Goddard Space Flight Center, Greenbelt, MD 20771, USA. [9]Laboratoire d'Études Spatiales et d'Instrumentation en Astrophysique, Observatoire de Paris, 92195 Meudon, France. [10]Université Côte d'Azur, Observatoire de la Côte d'Azur, Laboratoire Lagrange CNRS, 06304 Nice, France. [11]Planetary Science Institute, Tucson, AZ 85719, USA. [12]Lunar and Planetary Laboratory, University of Arizona, Tucson, AZ 85721, USA. [13]Sapienza University of Rome, 00185 Rome, Italy. [14]California Institute of Technology, Pasadena, CA 91125, USA. [15]National Space Institute, Technical University of Denmark, 2800 Kongens Lyngby, Denmark. [16]Department of Earth and Planetary Sciences, Weizmann Institute of Science, Rehovot 76100, Israel. [17]Cornell University, Ithaca, NY 14853, USA. [18]Institute for Astronomy, University of Hawaii at Manoa, Honolulu, HI 96822, USA. [19]Malin Space Science Systems, San Diego, CA 92121, USA. [20]Center for Space Technology and Research, Georgia Institute of Technology, Atlanta, GA 30332, USA. [21]Department of Atmospheric and Oceanic Sciences, University of California, Los Angeles, CA 90095, USA. [22]Laboratory for Atmospheric and Space Physics, University of Colorado, Boulder, CO 80303, USA.
*Corresponding author. Email: sbolton@swri.edu

cloud deck to be illuminated on the nightside this far beyond the terminator. Juno cannot determine whether this is detached high-altitude haze or a towering cloud column whose base is shadowed.

The deep atmosphere

The MWR measures thermal emission upwelling from previously unexplored depths in Jupiter's atmosphere (*11*, *12*). Its two main scientific objectives are to determine the global abundance of ammonia and water and to observe dynamical features in the deep atmosphere. Most of our current knowledge of temperatures, winds, composition, and cloud properties is confined to the tops of the clouds (i.e., to pressures of 0.5 bar or less). The Galileo probe measured atmospheric properties down to the 22-bar level at one point on the planet, and therefore did not provide a global view (*13*, *14*). In contrast, the MWR comprises six radiometric channels operating at wavelengths from 1.4 to 50 cm that collectively sample the thermal emission from pole to pole with better than 1° resolution in latitude at the equator, and from the cloud tops to pressures as deep as several hundred bars.

During a perijove pass, the MWR antennas scan north to south along the subspacecraft track as the spacecraft spins at 2 rpm along its orbit, obtaining overlapping measurements of the thermal radiances of each point along the track at 100-ms intervals. The radiances are converted by Planck's law to a blackbody temperature and are accordingly given in units of kelvin (*15*). Further, the measurements have been corrected for finite beam effects to obtain a source brightness temperature, or the effective mean radiance of Jupiter in the beam at the boresight axis, for each observation. The absolute accuracy of each measurement is 2% (uncorrelated among channels), whereas the relative accuracy (variation with respect to latitude and emission angle) at each wavelength is 0.1%.

Figure 2 shows plots of Jupiter's nadir brightness temperatures for all six channels, obtained during Juno's first two observational passes of Jupiter on 27 August 2016 [perijove 1 (PJ1)] and 11 December 2016 (PJ3). Only the nadir brightness is shown and used in our analysis, although the dependence of brightness on emission angle has been used to identify and eliminate data with suspected systematic errors. The brightness at each wavelength depends on the mean temperature of the atmosphere responsible for the emission, which in turn depends on the vertical distribution of opacity. The mean pressure sampled at each wavelength is indicated in the figure. Details of the radiative transfer calculations and the identification of systematic errors are given in the supplementary materials. Brightness structure with latitude is observed at all wavelengths down to ~300 bars but is seen predominantly within 20° of the equator. Comparison of PJ1 and PJ3 brightness indicates that longitudinal variations are further confined to a "weather layer" at pressures less than ~9 bars. Strong correlations among wavelengths are observed in both passes near the region of the Equatorial Zone (±5° latitude) and North Equatorial Belt (NEB, 5° to 20°N) at all wavelengths. The repeatability of measured brightness at high latitudes and pressure depths greater than 10 bars demonstrates both that the atmosphere is stable in these regions and that the measurements are repeatable to at least the 1% level, or approximately the widths of the lines plotted in Fig. 2 (the small dip in the Ch. 1 data for PJ3

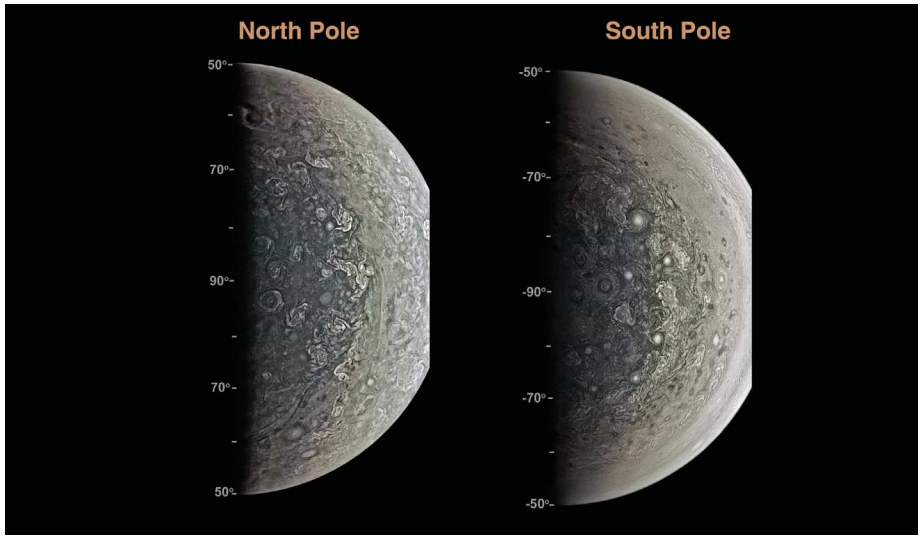

Fig. 1. Orthographic projection of JunoCam color composite images of the north and south polar regions of Jupiter obtained 27 August 2016. The north polar image was taken at 11:59 UT when the spacecraft was 73,009 km from Jupiter's cloud deck; the south polar image was taken at 13:56 UT when the spacecraft was 95,096 km from the cloud deck.

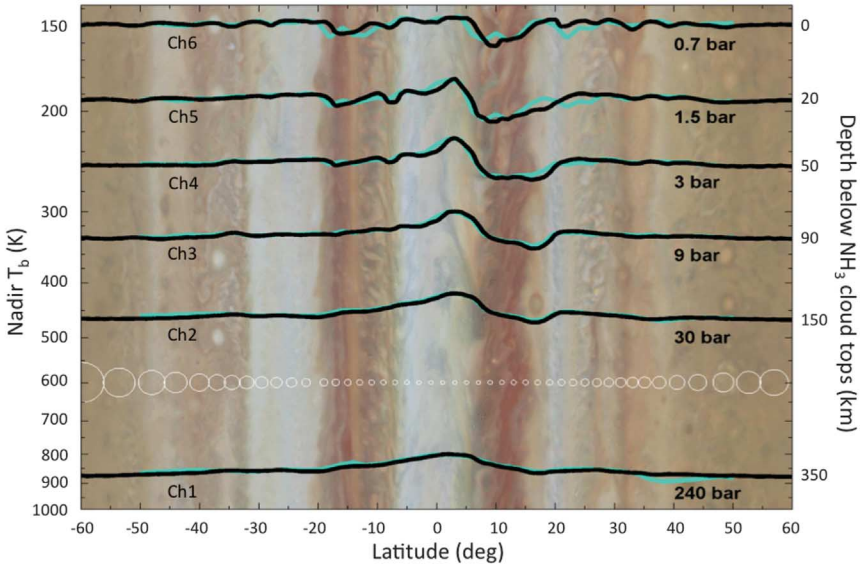

Fig. 2. Nadir brightness temperatures in the six channels of the MWR versus planetocentric latitude. The black and green curves are from the perijove passes on 27 August 2016 and 11 December 2016, for which the closest approaches were at 13:44 UTC and 17:05 UTC, respectively. The corresponding longitudes at equator crossing were 97°W and 7°W (system III). The frequencies of channels 1 to 6 are 0.6, 1.2, 2.6, 5.2, 10, and 22 GHz, respectively. Brightness temperature in kelvin is given at the left. Estimates of the pressure where the physical temperature is equal to the average brightness temperature are given below each curve. Underlying the plots of brightness temperature is a section of a Jupiter map taken by HST on 10 February 2016, in the visible wavelength range (PIA19643). The latitude of the bands has not changed during the months between the two data sets, but the longitudes of individual features have changed beyond the limits of the image. The white circles indicate the footprint sizes for channels 3 to 6, for which the full width at half power is 12° (these are shown sparsely for illustration, but the observations are in fact continuous in latitude). Channels 1 and 2 have full width at half power of 20°. The footprint size reflects the changing altitude of the spacecraft during its ~1-hour pass above the planet from north to south.

at 40°N is due to contamination by synchrotron emission).

We argue that the ~50 K variations of brightness temperature shown in Fig. 2 are due to variations of microwave opacity. As shown in the supplementary materials, if they were due to variations of physical temperature, the wind velocities at the equator would be greater than those observed by two orders of magnitude. Ammonia is by far the dominant source of microwave opacity in Jupiter's molecular atmosphere, surpassing that of water vapor by more than an order of magnitude and all other sources by much more (*16*). Therefore, we solve for the ammonia distribution that best matches the observed brightness measurements from PJ1. In doing so, we assume that the temperature profile follows a moist adiabatic lapse rate within the clouds and transitions to a dry adiabat below at a pressure that depends on atmospheric composition (*17*). The results are shown in Fig. 3.

The features seen in Fig. 3 are both striking and unexpected. The dominant equatorial plume and the desiccated gas in the neighboring NEB down at least to the 60-bar pressure level resemble a giant Hadley cell. However, the ammonia crystals that fall out of the clouds evaporate before they reach the 1.5-bar pressure level. The structure is a Hadley cell without rain. Traditionally, but on the basis of marginal direct evidence, the ammonia has been assumed to be uniformly mixed below the clouds, with perhaps a transition region from a few bars up to its saturation level of 0.7 bar (*18*). The present results indicate that this is not the case, with the region of uniformly mixed ammonia confined to the region below 60 bars where it asymptotically approaches a level of 350 parts per million by volume (ppmv). We have examined modeling and experimental errors that affect our estimate, including 2% absolute uncertainties in measured brightnesses, H_2O concentration varying by a factor of 10 relative to solar abundance, variations in the adiabat, uncertainties in NH_3 opacity, and uncorrected sidelobe contributions. We arrive at a net uncertainty in the derived ammonia concentration of ±30 ppmv, whereas the depicted ammonia concentration is seen to vary by a factor of 2 (e.g., from 350 ppmv down to 175 ppmv).

Hot spots

The Jovian Infrared Auroral Mapper (JIRAM) provides infrared images and spectra of Jupiter's thermal emission (*19*). Using its dedicated imager channel on the M band (4.5 to 5.0 μm), JIRAM mapped Jupiter's upper troposphere. The coverage is almost complete between 75°N and 75°S latitude. The map in Fig. 4 was obtained by superimposing about 1000 images with variable resolution (down to a few tens of kilometers) taken during more than 1 day of observations. The mapping does not take into account the wind motion of the features, as adjacent zones are mapped one after the other, usually 30 s apart.

JIRAM geometric data are given in system III coordinates (*20*). The brighter regions in Fig. 4 represent areas on Jupiter where thermal radiation escapes from pressure depths deeper than a few bars. These atmospheric emissions are mostly determined by reduced opacity of the widely spread clouds. Such a low opacity allows us to probe the composition of the troposphere below the reference level of 1 bar. Those "hot spots" are thought to be areas of downwelling and hence dry air. Many hot spots occur in a zone between 5° and 20°N, within the NEB, but "excess" thermal radiation is seen from much of the planet (*21*, *22*).

Mapping the water content inside hot spots to an unprecedented spatial resolution provides information on the cycles of condensable species and cloud formation mechanisms. The hot spot where the water relative humidity has been retrieved and reported can be seen in Fig. 4 at about 7°N latitude, 130° longitude. The retrieval code based on the preliminary results (*21*) has been developed and allows reconstruction of the humidity. Results indicate a strong latitudinal dependence in the humidity distribution, a pattern that is recurrent in almost all hot spots investigated. Inside the hot spot, the relative humidity is lower than 3%. Results on the distribution of water and ammonia confirm a downwelling of the air in the center of the hot spot and upwelling at its edges. Values of water vapor relative humidity retrieved from the analysis of JIRAM data are typically between 5 and 8 times the values previously reported (*25*) for the brightest parts of hot spots. However, these values remain rather small (below 10% in the entire area around the hot spot), therefore confirming the view of these structures as dry regions in the Jupiter atmosphere. Notably, analysis of two different hot spots from JIRAM data (*22*) clearly shows variable contents of water vapor between different hot spots. Consequently, although differences between our results and those reported in (*23*) may be partially due to different retrieval methods (including adopted databases or the inclusion of a deep liquid water cloud), both analyses agree that hot spots vary over a wide range of relative humidity.

Gravity field

The Jupiter gravity field was estimated from its effect on the Juno trajectory by measuring the Doppler shift of Juno's radio signal acquired by the NASA Deep Space Network. Juno's polar orbit and extremely low perijove make it much more sensitive to Jupiter's gravity field than those of previous missions.

For the initial science perijove (PJ1), the tracking station transmitted a signal at X-band (8 GHz). The spacecraft transponder coherently locked to this signal and transmitted signals back at X-band and Ka-band (32 GHz). With a low level of solar activity at that time, the dual-frequency downlink could be used to calibrate for the effects of charged particles in the Io plasma torus. We also used data from PJ2 on 19 October 2016 when only X-band Doppler data were available.

The data were used to estimate the gravity field parameterized by zonal harmonics through

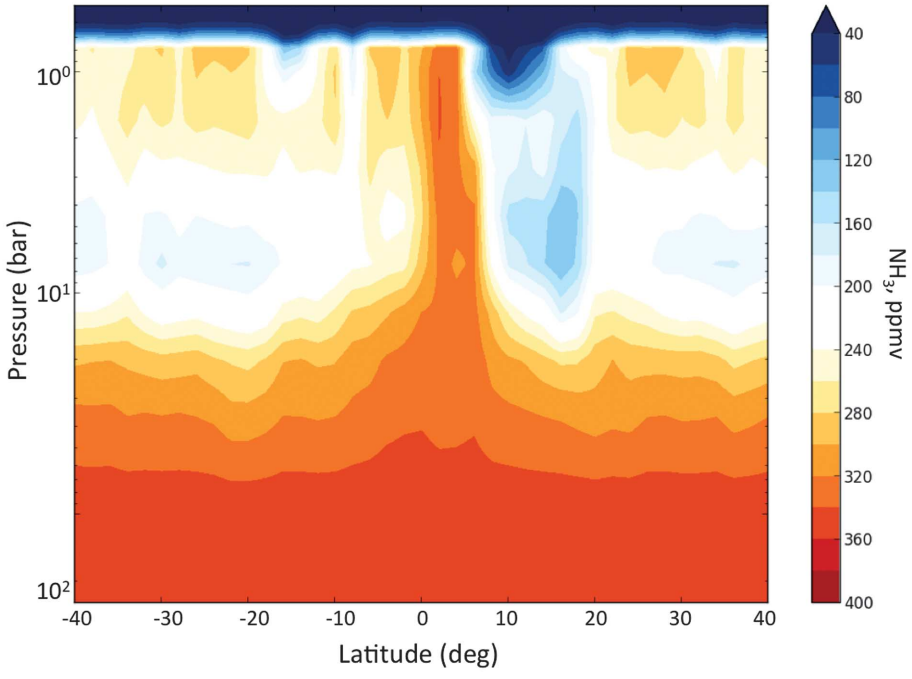

Fig. 3. Planetocentric latitude-altitude cross section of ammonia mixing ratio. The thin blue band at the top—near the 1-bar level—is where ammonia is condensing and the mixing ratio is low (<100 ppmv). The high mixing ratio at the equator is interpreted as air that is exchanging with the deep atmosphere at pressures of 100 bars or more, where the mixing ratio is 330 to 370 ppmv.

degree 12 plus sectoral and tesseral harmonics of degree 2, along with corrections to the Jupiter spin axis direction. The Juno data have less sensitivity to the Jupiter mass parameter (GM) than the data from the Galileo orbiter flybys of the Galilean satellites. We have applied a constraint to the Jupiter GM based on those data (*24*).

The estimated gravity harmonics are given in table S3. The odd zonal parameters for degree greater than 3 along with even zonal parameters J_{10} and J_{12} are not included in table S3 because the estimated values are well below the uncertainties. The uncertainties account for both the effect of the observed data noise and from possible systematic errors. Our uncertainties include the effect of a possible gravity field of degree and order 30, due to surface winds with depth of 10,000 km, that is not well sampled by data from two Juno orbits (*25*). (See the supplement for more details on the data noise and model used.)

Table S3 also includes earlier gravity field estimates from Pioneer and Voyager (*26*) and from a combination of the Pioneer and Voyager data with data from the Galileo mission (*27*) and with data from the Cassini and New Horizons missions (*28*). These are associated with ephemerides for the jovian satellites designated Jup230 and Jup310. Unlike the Juno results presented here and the earlier Pioneer and Voyager analyses, the uncertainties for Jup230 and Jup310 do not account for possible systematic errors. The uncertainties for the Juno data ignoring systematic errors are about one order of magnitude smaller than the uncertainties given here. Aside from the differences in development of uncertainties, the estimated coefficients are generally in agreement within uncertainties. The uncertainties in J_4 and J_6, key parameters for constraining jovian interior models, are improved with the Juno data over earlier estimates by factors of 5 and 22, respectively. The estimated values of J_4 and J_6 from the Jup310 solution differ from the other solutions by more than twice the Jup310 estimated uncertainties. This is thought to be due to systematic errors in photographic observations of Amalthea by Cassini and New Horizons.

Current published interior models do not agree precisely with the Juno data, although Nettelmann *et al.*'s model (*29*) is close because they were fitting to values of J_4 and J_6 from a previous determination by Jacobson (*27*) that are close to the Juno values. Figure 5 shows the derived values of J_4 and J_6 from recent models, all of which have J_2 consistent within the uncertainty of the Juno determination, along with previous and current estimates of J_4 and J_6. At the level of accuracy provided by the Juno measurements, differential rotation can affect these harmonics (*30*). We expect to get a better understanding of differential rotation by looking at small higher harmonics (e.g., J_8, J_{10}) and the odd harmonics that do not exist in hydrostatic equilibrium (e.g., J_3). The models have varying interior temperatures, heavy element distributions, and core masses. Some of the differences in predicted gravity arise from uncertainties in the equation of state for hydrogen-helium mixtures, the assumption of an adiabatic interior and the effects of helium immiscibility. Wahl *et al.* (*31*) presented a possible interpretation for the Juno data that requires a core that is dispersed out to perhaps as much as 0.5 R_J. An assessment of this and other possibilities must await additional Juno observations. The

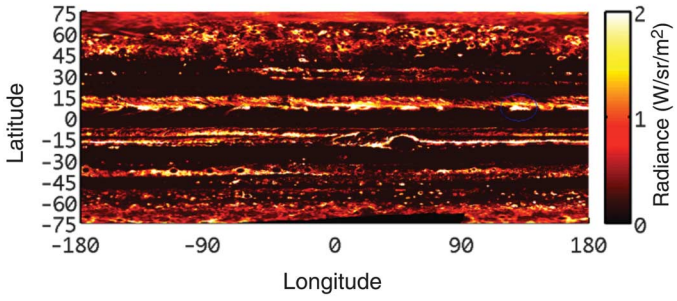

Fig. 4. Cylindrical map of the infrared emission from Jupiter as detected by JIRAM. The map is colored according to radiance in W m^{-2} sr^{-1} integrated from 4.5 to 5.0 μm. System III reference frame is used.

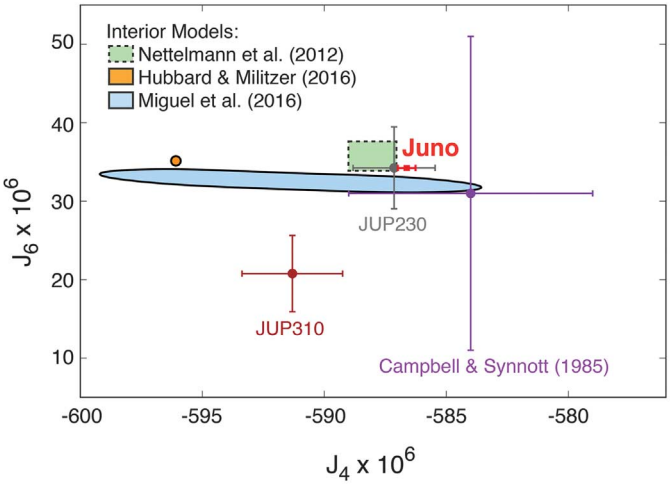

Fig. 5. Jupiter gravitational field coefficients J_4 and J_6. Pre-Juno observations from Campbell and Synnott (1985) (*26*) (purple), Jacobson (2003) (*27*) (JUP230, gray), and Jacobson (2013) (*28*) (JUP310, brown) are compared to Juno's preliminary measurement (red); values are given in table S3. Overlain are model predictions by Nettelmann *et al*. (2012) (*29*), Hubbard and Militzer (2016) (*39*), and Miguel *et al*. (2016) (*40*).

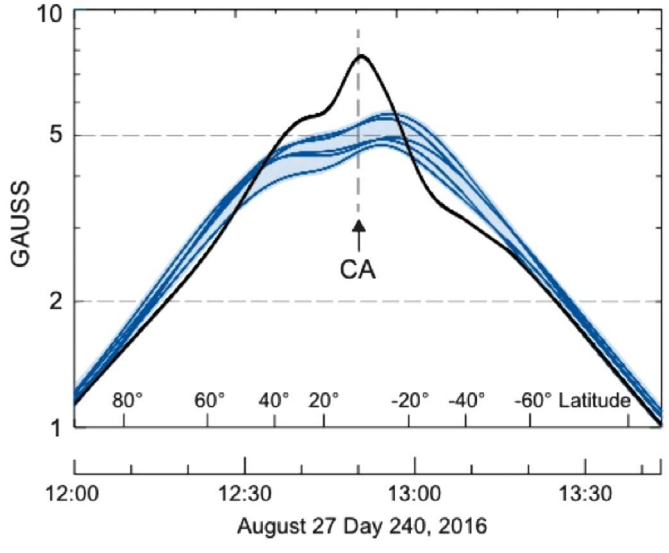

Fig. 6. Magnitude of the magnetic field observed along Juno's closest approach trajectory (solid line) as a function of time and spacecraft latitude, compared with that computed from a suite of existing models. The stippled region illustrates the range of such model predictions, bounded by the VIP4 model beneath and the GSFC O4 model above.

addition of heavy elements, in particular water, is important and we expect to place constraints on this from the microwave observations. Magnetic field data may also reduce the ambiguity of interpretation.

Magnetic field

The Juno spacecraft ventured closer to Jupiter's surface than previous spacecraft, passing to within 1.06 R_J of its center on its pole-to-pole trajectory. Juno's magnetometer (*32*) sampled at a rate of 64 vector samples/s throughout its closest approach, recording a magnetic field that greatly exceeded expectations based on existing models (Fig. 6). The maximum magnetic field observed during this periapsis was 7.766 G, more than an order of magnitude greater than Earth's maximum (south polar) surface field magnitude (0.66 G). The observed magnetic field displays more spatial variation relative to that represented by low degree and order spherical harmonic models, indicative of a rich harmonic content awaiting Juno's mapping phase. Juno's mapping phase is designed to envelop Jupiter in a dense net of observations equally distributed in longitude, and this initial pass indicates that the mapping phase will reveal a field rich in higher harmonics.

Although many spacecraft have sampled Jupiter's powerful magnetic field, none have sampled the field well inside of Io's orbit (5.95 R_J) since the flybys of Pioneer 10 and Pioneer 11 during the early 1970s. Our knowledge of Jupiter's magnetic field is thus limited by a paucity of direct observation close to the planet's surface, reflected in spherical harmonic models (*33*, *34*) that are confined to low degree and order, typically 3 or 4. The model field in widespread use and adopted by the Juno Project uses observations of the Io flux tube footprint as an additional constraint, but even so, this model's degree and order 4 terms are only partially resolved. Figure 6 compares the observed field magnitude with that calculated from a suite of such models (*34*), demonstrating that none adequately characterize the field near the surface.

Characterization of the field to high degree and order allows one to estimate the depth to the dynamo region, under the assumption that the harmonic spectrum is essentially "white" at the core surface—that is, represented by harmonic terms of equal amplitude by degree. Earth's dynamo radius (~0.5 R_E) may be located in this way and is consistent with seismic observations of the fluid core. The dynamo surface may also be located using the frozen flux theorem if variation of the magnetic field with time can be detected. The rich harmonic content indicated by Juno's initial (instrumented) periapsis pass portends a dynamo generation region not far beneath the surface. This may indicate that dynamo generation in Jupiter's interior—a process that requires electrically conducting fluid in convective motion—may occur in the molecular hydrogen layer above the pressure-induced transition to the metallic state, as first suggested by Smoluchowski (*35*). Experimental data (*36*) indicate substantial electrical conductivity in dense molecular hydrogen. Theoretical estimates consistent with these data (*37*) allow for a conductivity $\sigma \sim 1.5 \times 10^5$ S/m at 0.89 R_J and $\sigma \sim 1.5 \times 10^3$ S/m at 0.93 R_J. These values suggest a magnetic Reynolds number of $Re_m \equiv \mu_0 \sigma v L \sim 10^3$ to 10 for these radii, where μ_0 is the permeability of free space, assuming a characteristic fluid velocity $v \sim 0.01$ m/s and characteristic length scale $L \sim 1000$ km, both plausible choices for dynamo generation in Jupiter (*38*).

Summary

The results from Juno's initial close passes of Jupiter are changing our understanding of this gas giant. Juno's direct glimpse of Jupiter's poles shows numerous cyclonic storms clustered together and a storm illuminated in Jupiter's nightside that provided a measurement of its vertical extent. The deep microwave sounding of Jupiter by Juno demonstrates the power of this technique for unveiling spatial and temporal structure in the ammonia abundance. The initial measurement of Jupiter's gravity will inform interior models with implications for the extent, existence, and mass of Jupiter's core. The magnitude of the observed magnetic field observed was 7.766 G, almost twice as strong as expected. More results from Juno's initial passes are discussed in a companion paper (*1*).

REFERENCES AND NOTES

1. J. E. P. Connerney *et al.*, *Science* **356**, 826–832 (2017).
2. C. J. Hansen *et al.*, *Space Sci. Rev.* 10.1007/s11214-014-0079-x (2014).
3. T. Gehrels, in *Jupiter: Studies of the Interior, Atmosphere, Magnetosphere and Satellites*, T. Gehrels, Ed. (Univ. of Arizona Press, 1976), pp. 531–563.
4. E. García-Melendo, A. Sanchez-Lavega, *Icarus* **152**, 316–330 (2001).
5. X. S. Asay-Davis, P. S. Marcus, M. H. Wong, I. de Pater, *Icarus* **211**, 1215–1232 (2011).
6. A. P. Ingersoll *et al.*, *Nature* **280**, 773–775 (1979).
7. D. A. Godfrey, *Icarus* **76**, 335–356 (1988).
8. N. Barrado-Izagirre, S. Perez-Hoyos, A. Sanchez-Lavega, *Icarus* **202**, 181–196 (2009).
9. A. Antuñano, T. del Río-Gaztelurrutia, A. Sánchez-Lavega, R. Hueso, *J. Geophys. Res.* **120**, 155–176 (2015).
10. U. A. Dyudina *et al.*, *Icarus* **202**, 240–248 (2009).
11. M. A. Janssen *et al.*, *Icarus* **173**, 447–453 (2005).
12. M. A. Janssen *et al.*, *Space Sci. Rev.* 10.1007/s11214-017-0349-5 (2017).
13. W. M. Folkner, R. Woo, S. Nandi, *J. Geophys. Res.* **103**, 22847–22855 (1998).
14. M. H. Wong, P. R. Mahaffy, S. K. Atreya, H. B. Niemann, T. C. Owen, *Icarus* **171**, 153–170 (2004).
15. M. A. Janssen, Ed., *Atmospheric Remote Sensing by Microwave Radiometry* (Wiley, 1993).
16. P. G. Steffes *et al.*, *Space Sci. Rev.* 10.1007/s11214-016-0265-0 (2017).
17. C. Li *et al.*, *Geophys. Res. Lett.* 10.1002/2017GL073159 (2017).
18. S. K. Atreya, A. S. Wong, K. H. Baines, M. H. Wong, T. C. Owen, *Planet. Space Sci.* **53**, 498–507 (2005).
19. A. Adriani *et al.*, *Space Sci. Rev.* 10.1007/s11214-014-0094-y (2014).
20. B. A. Archinal *et al.*, *Celestial Mech. Dyn. Astron.* **109**, 101–135 (2010).
21. G. Sindoni *et al.*, *Geophys. Res. Lett.* 10.1002/2017GL072940 (2017).
22. D. Grassi *et al.*, *Geophys. Res. Lett.* 10.1002/2017GL072841 (2017).
23. M. Roos-Serote, S. K. Atreya, M. K. Wong, P. Drossart, *Planet. Space Sci.* **52**, 397–414 (2004).
24. R. Jacobson, R. Haw, T. McElrath, P. Antreasian, *Adv. Astronaut. Sci.* **103**, 465–486 (1999).
25. M. Parisi, E. Galanti, S. Finocchiaro, L. Iess, Y. Kaspi, *Icarus* **267**, 232–242 (2016).
26. J. K. Campbell, S. P. Synnott, *Astrophys. J.* **90**, 364–372 (1985).
27. The JUP230 solution corresponds to the gravity field of Jupiter calculated by R. A. Jacobson in 2003 using Pioneer, Voyager, and Galileo data as released on http://ssd.jpl.nasa.gov/?gravity_fields_op
28. The JUP310 solution corresponds to the gravity field of Jupiter calculated by R. A. Jacobson in 2013 using Pioneer, Voyager, Galileo, and New Horizons data as released on http://ssd.jpl.nasa.gov/?gravity_fields_op
29. N. Nettelmann, A. Becker, B. Holst, R. Redmer, *Astrophys. J.* **750**, 52 (2012).
30. Y. Kaspi *et al.*, *Geophys. Res. Lett.* 10.1002/2017GL073629 (2017).
31. S. Wahl *et al.*, *Geophys. Res. Lett.* 10.1002/2017GL073160 (2017).
32. J. E. P. Connerney *et al.*, *Space Sci. Rev.* 10.1007/s11214-017-0334-z (2017).
33. J. E. P. Connerney, M. H. Açuna, N. F. Ness, T. Satoh, *J. Geophys. Res.* **103**, 11929–11939 (1998).
34. J. E. P. Connerney, in *Treatise on Geophysics, Volume 10: Planets and Satellites*, G. Schubert, T. Spohn, Eds. (Elsevier, 2015), pp. 195–237; https://ntrs.nasa.gov/archive/nasa/casi.ntrs.nasa.gov/20150011017.pdf.
35. R. Smoluchowski, *Astrophys. J.* **200**, L119–L121 (1975).
36. W. J. Nellis, S. T. Weir, A. C. Mitchell, *Science* **273**, 936–938 (1996).
37. M. French *et al.*, *Astrophys. J. Suppl. Ser.* **202**, 5 (2012).
38. T. Guillot, D. J. Stevenson, W. B. Hubbard, D. Saumon, in *Jupiter*, F. Bagenal, T. Dowling, W. B. McKinnon, Eds. (Cambridge Univ. Press, 2004), chap. 3.
39. W. B. Hubbard, B. Militzer, *Astrophys. J.* **820**, 80 (2016).
40. Y. Miguel, T. Guillot, L. Fayon, *Astron. Astrophys.* **596**, A114 (2016).

ACKNOWLEDGMENTS

We acknowledge the important contributions of M. H. Acuña, A. Coradini, and M. J. Klein to the Juno project. The images in Fig. 1 were processed by citizen scientist R. Tkachenko as part of Juno's outreach program. The visible map shown in Fig. 2 is based on observations made with the NASA/ESA Hubble Space Telescope (HST) under program GO14334, the Outer Planet Atmospheric Legacy Program. Support for the Juno project is provided under NASA grant NNM06AA75C to Southwest Research Institute; NASA grant NNN12AA01C to the Jet Propulsion Laboratory/Caltech; Centre National d'Études Spatiales (T.G. and Y.M.); and Agenzia Spaziale Italiana (ASI) (A.A., D.G., L.I., and A.M.). The JIRAM and Ka-band instruments are funded by ASI; HST is funded by NASA through a grant from the Space Telescope Science Institute, which is operated by the Association of Universities for Research in Astronomy Inc. under NASA contract NAS5-26555. All maps from this program can be retrieved at https://archive.stsci.edu/prepds/opal/. Supporting data are available in the supplementary materials. As agreed with NASA, fully calibrated Juno data are released on schedule via the NASA Planetary Data System at https://pds.nasa.gov/.

SUPPLEMENTARY MATERIALS

www.sciencemag.org/content/356/6340/821/suppl/DC1
Materials and Methods
Figs. S1 to S4
Tables S1 to S4
References (*41*–*61*)

13 December 2016; accepted 1 May 2017
10.1126/science.aal2108

Science

Jupiter's interior and deep atmosphere: The initial pole-to-pole passes with the Juno spacecraft

S. J. Bolton, A. Adriani, V. Adumitroaie, M. Allison, J. Anderson, S. Atreya, J. Bloxham, S. Brown, J. E. P. Connerney, E. DeJong, W. Folkner, D. Gautier, D. Grassi, S. Gulkis, T. Guillot, C. Hansen, W. B. Hubbard, L. Iess, A. Ingersoll, M. Janssen, J. Jorgensen, Y. Kaspi, S. M. Levin, C. Li, J. Lunine, Y. Miguel, A. Mura, G. Orton, T. Owen, M. Ravine, E. Smith, P. Steffes, E. Stone, D. Stevenson, R. Thorne, J. Waite, D. Durante, R. W. Ebert, T. K. Greathouse, V. Hue, M. Parisi, J. R. Szalay and R. Wilson

Science **356** (6340), 821-825.
DOI: 10.1126/science.aal2108

Juno swoops around giant Jupiter

Jupiter is the largest and most massive planet in our solar system. NASA's Juno spacecraft arrived at Jupiter on 4 July 2016 and made its first close pass on 27 August 2016. Bolton *et al.* present results from Juno's flight just above the cloud tops, including images of weather in the polar regions and measurements of the magnetic and gravitational fields. Juno also used microwaves to peer below the visible surface, spotting gas welling up from the deep interior. Connerney *et al.* measured Jupiter's aurorae and plasma environment, both as Juno approached the planet and during its first close orbit.

Science, this issue p. 821, p. 826

www.sciencemag.org/content/356/6340/821/suppl/DC1

Supplementary Materials for

Jupiter's interior and deep atmosphere: The initial pole-to-pole passes with the Juno spacecraft

S. J. Bolton,* A. Adriani, V. Adumitroaie, M. Allison, J. Anderson, S. Atreya, J. Bloxham, S. Brown, J. E. P. Connerney, E. DeJong, W. Folkner, D. Gautier, D. Grassi, S. Gulkis, T. Guillot, C. Hansen, W. B. Hubbard, L. Iess, A. Ingersoll, M. Janssen, J. Jorgensen, Y. Kaspi, S. M. Levin, C. Li, J. Lunine, Y. Miguel, A. Mura, G. Orton, T. Owen, M. Ravine, E. Smith, P. Steffes, E. Stone, D. Stevenson, R. Thorne, J. Waite, D. Durante, R. W. Ebert, T. K. Greathouse, V. Hue, M. Parisi, J. R. Szalay, R. Wilson

*Corresponding author. Email: sbolton@swri.edu

Published 26 May 2017, *Science* **356**, 821 (2017)
DOI: 10.1126/science.aal2108

This PDF file includes:

Materials and Methods

Microwave Radiometer

The Juno Microwave Radiometer (MWR) comprises six separate radiometers (channels 1-6) that operate at frequencies distributed approximately by octave from 600 MHz to 22 GHz (50 to 1.2 cm wavelength) respectively, as listed in Table S1. Each channel obtains contiguous measurements of the antenna temperature T_a at 100-ms intervals with the uncertainties given in the table. Since the spacecraft spins at 2 rotations per minute, observations are taken at spacecraft clock angle increments of 1.2°. Given the antenna beamwidths in the table, this amounts to 10 or more observations per MWR footprint on Jupiter. Allowing for averaging of adjacent measurements and the typical source temperature at each wavelength, the intrinsic instrument noise in the nadir brightness temperatures shown in Figure 2 are negligible compared to the relative and absolute errors of 0.1% and 2% respectively.

At the longest-wavelength channels, particularly channel 1, synchrotron emission from Jupiter's radiation belts becomes particularly strong and contamination of atmospheric measurements due to radiation from this source entering the antenna sidelobes must be corrected. Particular care in the design and implementation of the antennas was taken to minimize this source of error so that it does not limit our ability to measure the nadir brightness and its emission angle dependence. Figure S1 shows a validation of the design using data obtained during the PJ1 pass. This plot shows the calibrated antenna temperature obtained as a function of spacecraft clock angle with respect to nadir for channel 1, with the emission from both sources shown in context. Each horizontal line in the figure represents the contiguous antenna temperature measurements obtained during one rotation of the spacecraft as it sweeps from north to south across Jupiter, crossing closest to nadir at 0° clock angle, then sweeping around across the radiation belt in the opposite hemisphere. The vertical shape symmetric about 0 deg clock angle is Jupiter's thermal emission, while the bright signal in the rest of the sky is the synchrotron emission. The spurs of synchrotron radiation that begin to impinge on the planet near ±40° latitudes correspond to the north and south horns of radiation from mirror-point electrons that come close to the spacecraft at these latitudes. The separation of thermal atmospheric radiation from synchrotron emission appears complete in this image, although detailed calculations using the known antenna beam pattern show that a small contribution from the latter remains at the nadir line *(12)*. Nevertheless this contributes less than 1% to the atmospheric signal and is negligible for the nadir brightness analysis reported here, although the effect on emission angle dependence has not been corrected. The rapid decrease of the synchrotron emission with decreasing wavelength makes it negligible for nadir emissions in all other channels.

The calculations used to interpret the measurements make use of the Juno Atmospheric Microwave Radiative Transfer (JAMRT) code developed by the Juno project for this purpose *(12)*. Combined with a model of the atmosphere, JAMRT computes radiances from profiles of temperature, ammonia and water from the cloud tops down to pressures of 1000 bars. The model uses experimental data on the opacity of ammonia and water in hydrogen-helium mixtures at temperatures up to 600 K and pressures up to 100 bars *(18,*

41-43). The uncertainties of the opacity models have been determined to be about 5% to 7% from low pressures up to 100 bars. These determinations are supplemented by room-temperature data that range to several hundred bars *(44)*. The model allows for variations in pressure-temperature structure, variable concentrations of constituents in addition to water and ammonia gas that affect the opacity such as water/ammonia cloud droplets and NH_4SH (from H_2S reacting with NH_3). All brightness temperatures are computed assuming a one-dimensional line-of-sight integration from above the atmosphere with no scattering or refraction.

Figure S2 shows the brightness temperature contribution functions computed for the six MWR channels using JAMRT and an assumed atmosphere containing nominal concentrations of ammonia and water (3 × solar each), each assumed to be uniformly mixed up to their respective saturation levels and following a saturation curve above that. The contribution function is calculated here as the fractional contribution to the net brightness temperature per increment of log (P), so that the area under the curve for a given pressure range is proportional to the net thermal contribution from that range. The contribution functions are approximately symmetric in log (P) for channels 2 through 6 (24 to 1.37 cm), with peaks around 30, 10, 3.5, 1.5 and 0.7 bars respectively, and are generally contained within the region where the opacities of NH_3 and H_2O have been measured. The highest frequency lies in the center of the strong ammonia 1-cm band, and the remaining frequencies were chosen to provide overlapping weighting functions descending as far as feasible into Jupiter's depths. However, most of the contribution to channel 1 brightness temperatures depends on extrapolation by as much as two orders of magnitude in pressure beyond the range of laboratory measurements, and to temperatures in excess of 2000 K. While structure seen at this lowest frequency indicates very deep dynamics, its interpretation will have a different character than that from the other channels because the opacity at depth is more uncertain.

Comparison of PJ1 and PJ3 brightnesses indicates that longitudinal variations are further confined to a "weather layer" at pressures less than about 9 bars. The results are qualitatively consistent with the Galileo probe results, which have low values of the ammonia mixing ratio extending well below the ammonia cloud and then transitioning to a higher value deeper down. Figure 3 shows the transition occurring at a pressure of ~25 bar, but this is deeper by a factor of 3 in pressure than that observed by the Galileo probe. Juno's value for the NH_3 mixing ratio at 200 bars is 330-370 ppmv, whereas absorption of the Galileo probe radio signal gives 700±100 ppmv, and the Galileo probe mass spectrometer gives 568±215 ppmv (where we have converted from values relative to H_2 to those relative to the bulk mixture). The unexpected concentrations measured by the Galileo probe for both NH_3 and H_2O have been ascribed to its landing in an anomalous atmospheric region (a 5-micron hot spot). In the context of our results, we note that the probe descended into the atmosphere at 7° N just at the transition between the equatorial plume and the NEB ammonia-dry region, where the measurements would be expected to depend strongly on the exact location. This general location is a region of intermixed ascending ammonia-rich and descending ammonia-poor gas, and a single measurement cannot be expected to give a representative picture of Jupiter's composition for condensable gasses.

In inverting the data in Fig. 2, we assumed that the horizontal variations of brightness temperature are due to horizontal variations of opacity, i.e., ammonia, rather than horizontal variations of temperature. The rationale for this assumption is that real temperature variations $\Delta T(y, P)$, i.e., temperature variations at constant pressure, would lead to impossibly large wind speeds. Winds are connected to temperatures by the thermal wind equation

$$f\frac{\partial \bar{u}}{\partial \log P} = R\left(\frac{\partial T}{\partial y}\right)_P \qquad \text{(S1)}$$

Here f is the Coriolis parameter, $\bar{u}$ is the mean eastward velocity, R is the gas constant for the hydrogen-helium atmosphere, and y is the northward coordinate measured from the equator. This equation is valid when the horizontal dimensions of interest are much greater than the vertical dimensions, as they are in Fig. 3. Close to the equator f is equal to βy, where $\beta = 2\Omega/a$, Ω is the rotation rate, and a is the radius of the planet. We fit the brightness temperatures in Fig. 2 to a Gaussian of the form $T(y, P) = \Delta T \exp(-y^2/y_0^2)$, where $\Delta T = -40$ K and $y_0 = 5000$ km, about 4° of latitude. Left and right sides of Equation (1) vanish at the equator, so we use L'Hôpital's rule to obtain

$$\frac{\partial \bar{u}}{\partial \log P} = -\frac{2R\Delta T}{\beta y_0^2} \approx 2350 \text{ m s}^{-1} \qquad \text{(S2)}$$

Distributed over $\log P = 4.6$, about 2 orders of magnitude in P, the velocity at the top relative to that at the bottom of Fig. 3 would be -10800 m s^{-1}, which is impossibly large and of the wrong sign. Thus the brightness temperature differences cannot be due to $\Delta T(y, P)$ and must be due to opacity variations.

Gravity Field

Mission orbit geometry and gravity data

Key geometry information for the first two Juno perijoves following orbit insertion, designated PJ1 and PJ2, are given in Table S2. The orbit was nearly polar with orbit period 53 days. The time of perijove is given in barycentric dynamical time (TDB). The orbit plane was nearly perpendicular to the direction from Earth to Jupiter. Both perijoves were near solar conjunction. At perijove the height of the spacecraft above the 1-bar ellipsoid was about 4100 km at latitude 3.8° N and 4.7° N. The spacecraft was nearly over the north pole of Jupiter about one hour before perijove and above the south pole about one hour after perijove. When above the north and south poles the spacecraft was approximately one Jupiter radius above the 1-bar level.

For PJ1 the data used cover from 3.2 hours before perijove to 5.1 hours after perijove. For PJ2 the data covered from 3.1 hours before perijove to 2.8 hours after perijove. For both perijoves, the tracking station transmitted a radio signal to the spacecraft at X-band (8 GHz). A transponder on the spacecraft locked coherently in phase

onto the signal from the tracking station and transmitted a signal back to the tracking station.

For PJ1 the spacecraft transmitted signals at both X-band and at Ka band (32 GHz). The difference in the Doppler shift of the X-band and Ka-band signals were used to calibrate the effect of charged particles on the radio signal from the spacecraft to Earth. The only significant signature in this calibration is near the time of closest approach to Jupiter. Near perijove the spacecraft was inside the orbit of Io and the radio signal passed through the Io plasma torus. The Io plasma torus causes an effect on radio signals that has been previously measured from the Voyager and Ulysses spacecraft *(45, 46)*. We used the dual-frequency radio signal to Earth to calibrate the effect of the plasma torus, also applied, appropriately scaled, to the X-band radio signal from the tracking station to the spacecraft. We applied an estimate of the effect of the Io plasma torus to the PJ2 data based on the dual-frequency measurements from PJ1.

The data noise for PJ1 was dominated by a combination of fluctuations in the troposphere and antenna mechanical noise. The data noise for PJ2 was dominated by solar plasma but at lower level than expected *(47)*. The measurement noise for the two orbits is characterized by the Allan deviation *(48)* that measures the fractional frequency stability as a function of the integration time. For the Jovian gravity field estimation the main time scales of interest are from ~100 s to ~1000 s, for which the change in Doppler is caused by the zonal gravity harmonics from degree 2 to degree 12. Figures S3 and S4 show the Allan deviation for Doppler residuals. These are based on residuals after estimation of the relevant parameters. Data from the hour centered on perijove are excluded, since over that time the estimated parameters can absorb some of the measurement noise. The slope of the Allan deviation for PJ1 residuals over 100 s to 1000 s indicates white frequency noise, while for PJ2 the slope of Allan deviation indicates noise dominated by solar plasma. For PJ1 the slope of the Allan deviation indicates the Doppler measurements as a function of time are uncorrelated, while for PJ2 the Doppler measurements at different times have non-zero correlation as a function of the time between point. This correlation function can be calculated to provide the correct data weighting to use for estimation.

Gravity model and estimation technique

The mass distribution of a planet is generally different from that of a homogeneous spherical body. For this reason, the external gravitational potential of Jupiter can be conveniently expanded in series of spherical harmonics of degree *l* and order *m (49)*:

$$U(r,\lambda,\phi) = \frac{GM}{r}\sum_{n=0}^{\infty}\sum_{m=0}^{n}\left(\frac{R}{r}\right)^{n} P_{nm}(\sin\phi)\,[C_{nm}\cos(m\lambda) + S_{nm}\sin(m\lambda)] \qquad \text{(S3)}$$

where G is the gravitational constant, M and R are the mass and radius of Jupiter, r is the distance from Jupiter's center of mass, ϕ is the latitude, λ is the longitude, P_{nm} are the un-normalized associated Legendre functions, and C_{nm} and S_{nm} are the un-normalized spherical harmonic coefficients. The gravitational acceleration affecting the trajectory of Juno while orbiting about Jupiter can be calculated by taking the gradient of the

gravitational potential. In turn, spherical harmonics can be estimated by precise Doppler tracking of the spacecraft along with other relevant parameters.

The state vector x is the set of the estimated parameters. By means of radiometric observables z, it is possible to obtain a least-squares estimate x_c of the state vector, designed to combine a priori information and new data *(50)*:

$$x_c = \left(A^T W A + \tilde{\Lambda}\right)^{-1}\left(A^T W z + \tilde{\Lambda}\tilde{x}\right) \quad \text{(S4)}$$

where A is the matrix of observation partials, W is the observable weighting matrix, $\tilde{\Lambda}$ is the a priori information matrix and $\tilde{x}$ is an unbiased *a priori* estimate of the state vector. The quantity $P_{x,}$ given by:

$$P_x = \left(A^T W A + \tilde{\Lambda}\right)^{-1} \quad \text{(S5)}$$

is the covariance matrix, which bears information about the estimation accuracies. The square roots of the diagonal elements correspond to the formal uncertainties on the estimated parameters.

The measurements used for gravity analysis allow the estimation of a limited number of parameters, supported by the available data strength. However, unestimated parameters (for instance higher degree and order gravity harmonics) can be dynamically correlated with the estimated parameters and might undermine the filter accuracy and confidence in the estimated values and covariance.

One strategy to prevent the underestimation of the covariance is the technique of consider analysis. This approach features a set of parameters y which are not estimated, but whose a priori covariance P_y is used to augment the least-squares uncertainty. The consider covariance P_{CON} is given by:

$$P_{CON} = P_x + S P_y S^T \quad \text{(S6)}$$

where S is the sensitivity matrix:

$$S = \partial(x - x_c)/\partial y \quad \text{(S7)}$$

where $x - x_c$ is the difference between the true value of x and the least-squares estimate x_c. The consider covariance is composed of two positive definite terms: (i) the standard covariance matrix P_x; (ii) an additional component which depends on the sensitivity matrix and the a priori covariance for the consider parameters.

When data is accumulated (i.e. data available for more than one perijove) it is possible to adopt a multi-arc approach *(51)*, where the information from different arcs is combined. In this case, the formal uncertainties P_x will decrease because of the higher information content, while consider covariance P_{CON} can sometimes increase when estimated parameters are highly correlated with unestimated parameters.

Jovian gravity field estimation

The Doppler data from PJ1 and PJ2 were used to estimate the Jovian gravity field parameterized by zonal harmonics through degree 12 plus sectoral and tesseral harmonics of degree 2 along with corrections to the Jupiter spin axis direction and the initial position and velocity of the spacecraft for each perijove. The Juno data have less sensitivity to the Jupiter mass parameter (GM) than the data from the Galileo orbiter flybys of the Galilean satellites. We have applied a constraint to the Jupiter GM based on a fit to the Galileo orbiter data *(24)*. The a priori uncertainties for the other estimated parameters were set to be large compared with the final estimated uncertainties. The Jovian gravity field is also affected by tides raised by the Jovian satellites, with largest contribution by Io. Because the longitude of Juno with respect to Io was almost the same for PJ1 and PJ2 the data are not able to separate tide signature. Instead we have modeled the effect of tides using a value for the k_2 Love number of 0.379 from *Gavrilov and Zharkov (52)*. The tide model adds a time-averaged corrections $\Delta J_2 = 0.054\times10^{-6}$ and $\Delta C_{22} = 0.026\times10^{-6}$ that are small compared with the estimated uncertainties in J_2 and C_{22}.

The estimated gravity parameters are given in Table S3. The correlations between parameters are given in Table S4. The odd zonal parameters for degree greater than 3 along with J10 and J12 are not included in Table S3 since the estimated values are well below the uncertainties. The uncertainties listed account for both the effect of the observed data noise and from possible systematic errors using the consider analysis described above. The uncertainties include the effect of consider parameters describing a possible gravity field of degree and order 30 due to surface winds with depth of 10,000 km *(53)*. This results in gravity coefficient uncertainties that are fairly conservative but not an upper bound. The winds speeds used for this model are observed at the could tops, while to deeper winds may be larger. The only observation of Jovian wind speeds below the cloud levels from the Galileo probe were significantly larger than the cloud-top winds *(54)*.

The estimated values of the degree two sectoral and tesseral coefficients are well below the uncertainties. The values of C_{21} and S_{21} are zero if Jupiter's principal axis of inertia coincides with the spin axis. The values of C_{22} and S_{22} are zero if the mass distribution is symmetric about the rotation axis. These properties are expected for the fluid planet in equilibrium and have been used as constraints in some earlier analyses. The Juno data are strong enough to confirm these expectations.

Hot Spots

Starting from the preparatory work for the analysis of the JIRAM data from Grassi et al. *(55),* an end-to-end retrieval code based on the Bayesian formalism *(56)* was developed. The code is intended to study the composition of the upper troposphere in the pressure range 1-6 bars in Jupiter areas where a moderate cloud optical thickness ($\tau<2$) allows the thermal radiation to be emitted in this pressure range for measurements from space. The present code also includes a forward radiative transfer model based on correlated-k method *(57)*. Multiple scattering by clouds is also taken into account through a simple two-streams approach *(58)*.

The water, ammonia and phosphine abundances derived from JIRAM Hot Spot data reinforce the current view of the brightest parts of these areas as sites of prevailing descending vertical motions *(59)*. Nonetheless, possible evidence of upwelling is observed at the southern boundaries, as local enrichments in ammonia and phosphine along latitude rather than strictly correlated with 5μm radiance. Local minima of water relative humidity are also tentatively identified eastward of Hot Spot brightest parts, suggesting that Hot Spot IR morphology can be altered by clouds located higher than the 1.3-1 bar level assumed for the residual layer of ammonium hydrosulfide, consistently with the spacecraft visible observations discussed by *(60)* and *(61)*.

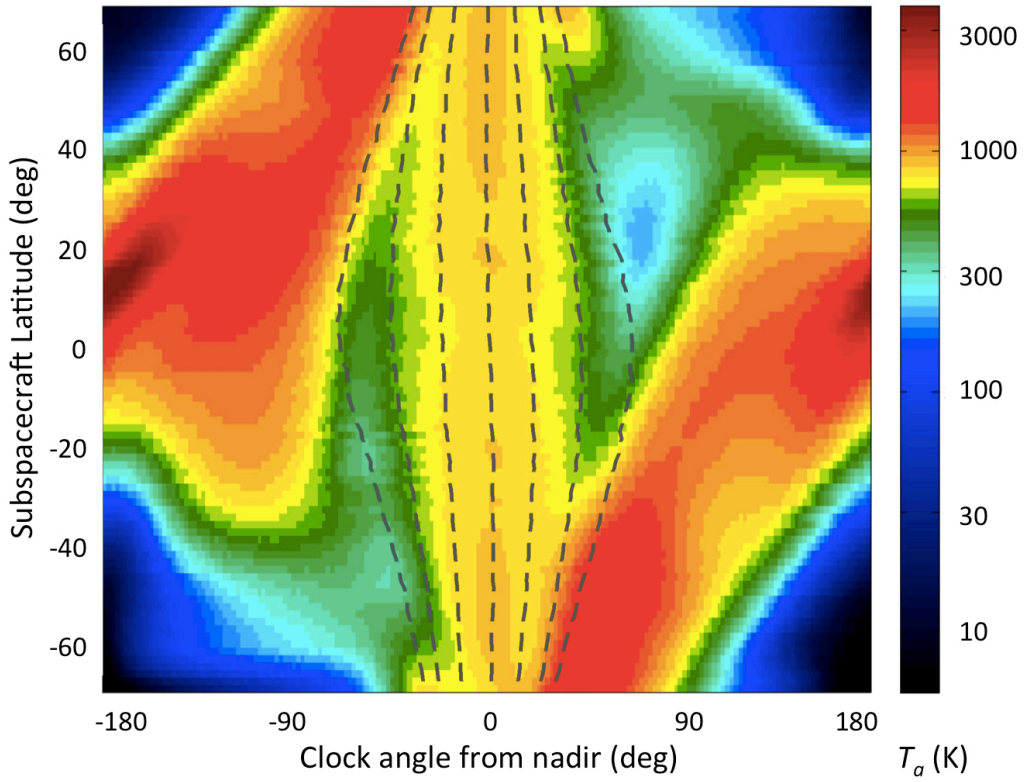

Fig. S1.

Channel 1 antenna temperature as a function of spacecraft clock angle through the perijove 1 pass. The dashed lines indicate lines of constant incidence angle at 0, 30, 60 and 90 degrees.

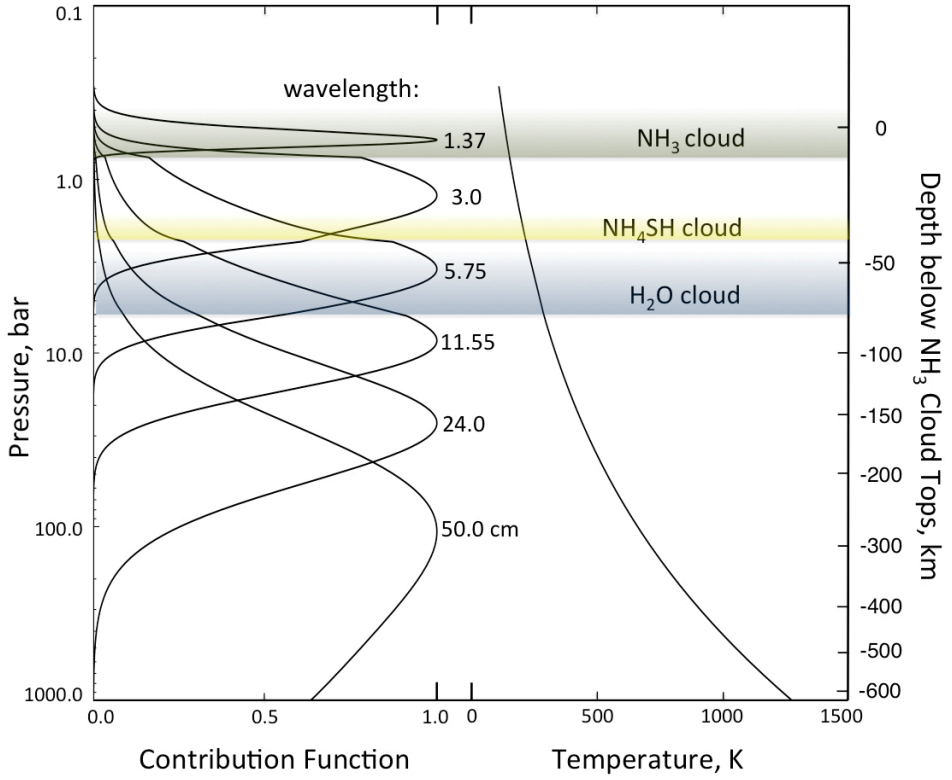

Fig. S2
Contribution functions for a nominal Jovian atmosphere at the MWR wavelengths and points for laboratory measurements of NH_3 and H_2O microwave opacity in context with a Jovian pressure-temperature profile.

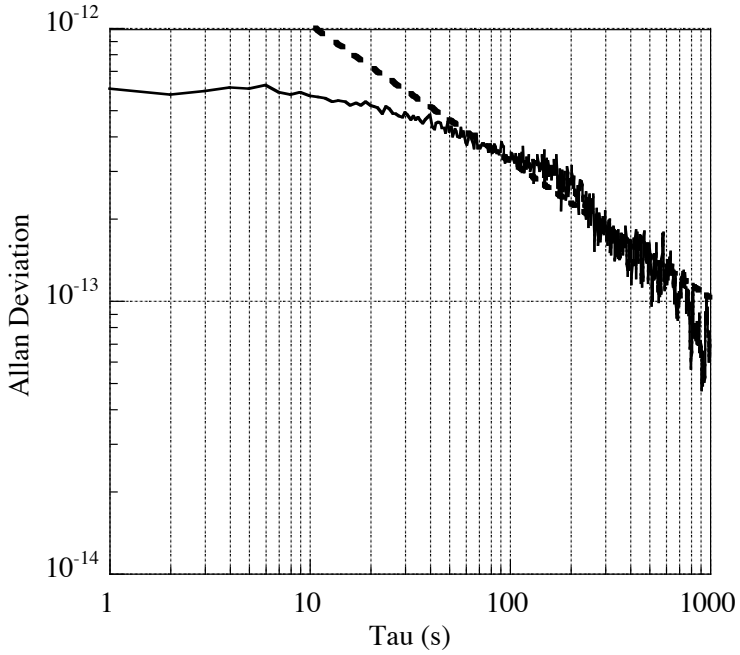

Fig. S3

The Allan deviation of the Doppler measurements from PJ1. For time scales from 100 to 1000 seconds the slope is approximately proportional to $tau^{-1/2}$ (dashed line) indicating the Doppler measurements are independent for those time scale.

.

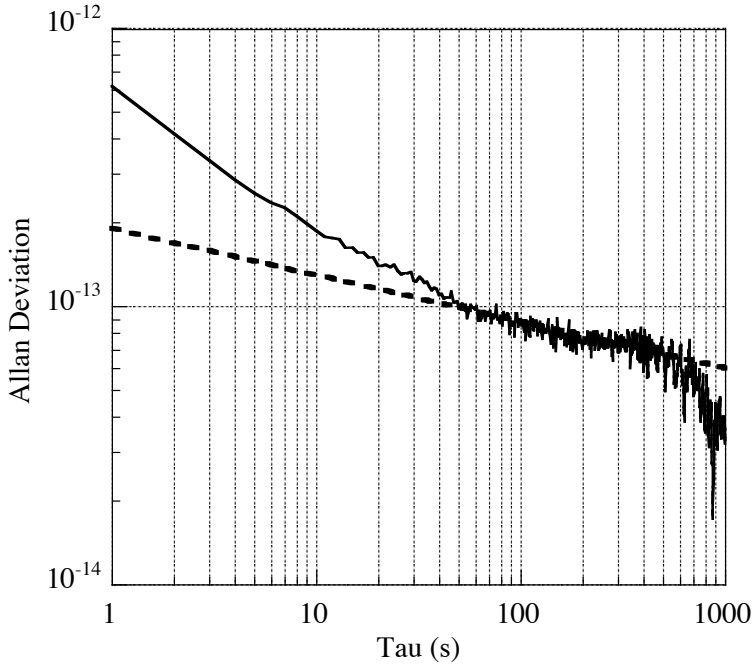

Fig. S4

The Allan deviation of the Doppler measurements from PJ2. For time scales from 100 to 1000 seconds the slope is approximately proportional to $tau^{-1/6}$ (dashed line) indicating the Doppler measurements are correlated on those time scales due to the character of solar plasma.

Table S1.

MWR antenna and receiver characteristics. ΔT_{noise} is the typical noise temperature for a 100 ms integration.

Channel	Frequency [GHz]	Wavelength [cm]	Beamwidth [deg]	ΔT_{noise} (100 ms) [K]
1	0.600	50	20.6°	0.59
2	1.248	24	21.0°	0.54
3	2.597	11.55	12.1°	0.42
4	5.215	5.75	12.1°	0.39
5	10.004	3.0	12.0°	0.21
6	21.900	1.37	10.8°	0.19

Table S2.

Geometry information for perijoves 1 and 2, including time of perijove, one-way light travel time LT from spacecraft to Earth, distance d from Juno to Earth, inclination *i*, of the orbit plane to Jupiter equator, height above Jupiter 1-bar ellipsoid at perijove *h*, latitude *l,* of perijove, angle *b* between orbit normal and direction from Earth to Jupiter, and angular separation SEP between the Sun and Jupiter as seen from Earth.

PJ	Time (TDB)	LT(min)	d(au)	i(°)	h(km)	λ(°)	β(°)	SEP(°)
1	2016 August 27 12:51:52	53.0	6.37	89.9	4147	3.8	2.8	22.6
2	2016 October 19 18:12:02	53.1	6.39	90.0	4179	4.7	9.4	18.2

Table S3.

Estimated Jovian gravity field parameters from Pioneer/Voyager and from Juno's first two science orbits combined. The zonal harmonics J_n and degree-2 tesseral harmonics $S_{i,j}$ and $C_{i,j}$ are unnormalized and dimensionless. The Jupiter spin axis direction given by Earth right ascension a and declination d at epoch 2000.0. The gravity harmonics from Pioneer and Voyager have been scaled from the Jupiter radius they used to the radius 71492 km adopted by Juno, whilst their pole direction has been converted from Earth-Mean-Equator of 1950 to Earth-Mean-Equator of 2000.

Parameter	Pioneer/Voyager	Jup230	Jup310	Juno PJ1&PJ2
GM(km^3/s^2)	126686537.5 ± 101	126686534.9 ± 1.5	126686534.2 ± 2.7	126686533.0 ± 2.0
J_2 x10^6	14697.3 ± 1	14696.43 ± 0.21	14695.62 ± 0.29	14696.514 ± 0.272
J_3 x10^6	1.4 ± 5	-0.64 ± 0.90		-0.067 ± 0.458
J_4 x10^6	-583.9 ± 5	-587.14 ± 1.68	-591.31 ± 2.06	-586.623 ± 0.363
J_6 x10^6	30.8 ± 20	34.25 ± 5.22	20.78 ± 4.87	34.244 ± 0.236
J_8 x10^6				-2.502 ± 0.311
C_{21} x10^6				0.026 ± 0.303
S_{21} x10^6				0.030 ± 0.368
C_{22} x10^6	-0.030 ± 0.150	0.007 ± 0.008	-0.010 ± 0.067	0.005 ± 0.170
S_{22} x10^6	-0.007 ± 0.150	-0.013 ± 0.009	-0.014 ± 0.061	-0.010 ± 0.214
α(deg)	268.058 ± 0.005	268.0566 ± 0.0002	268.0571 ± 0.0003	268.057 ± 0.002
δ(deg)	64.494 ± 0.002	64.4953 ± 0.0001	64.4958 ± 0.0001	64.496 ± 0.013

Table S4.

Correlation matrix for estimated Jovian gravity field parameters. The correlation matrix is symmetric so only the upper diagonal is shown.

	RA0	DEC0	C21	S21
GM5	-1.50E-03	5.53E-03	3.74E-04	-7.78E-03
RA0		-8.28E-01	-9.82E-01	2.67E-01
DEC0			7.31E-01	-7.57E-01
C21				-1.26E-01

	S21	C22	S22	J2
GM5	-7.78E-03	-6.69E-03	-5.62E-03	-3.14E-03
RA0	2.67E-01	6.75E-01	8.32E-01	3.47E-01
DEC0	-7.57E-01	-9.61E-01	-9.95E-01	-4.77E-01
C21	-1.26E-01	-5.65E-01	-7.35E-01	-3.45E-01
S21		8.74E-01	7.48E-01	3.80E-01
C22			9.48E-01	5.00E-01
S22				4.72E-01
J2				

	J3	J4	J6	J8
GM5	5.61E-03	2.94E-03	4.22E-03	3.93E-03
RA0	-5.07E-01	-5.73E-01	-5.77E-01	-6.29E-01
DEC0	7.57E-01	5.70E-01	6.67E-01	6.87E-01
C21	4.44E-01	5.17E-01	4.84E-01	5.47E-01
S21	-7.62E-01	-3.62E-01	-5.14E-01	-4.85E-01
C22	-8.32E-01	-5.14E-01	-6.24E-01	-6.31E-01
S22	-7.51E-01	-6.18E-01	-7.13E-01	-7.30E-01
J2	-3.21E-01	-3.16E-01	-3.17E-01	-3.45E-01
J3		3.90E-01	4.23E-01	4.47E-01
J4			8.33E-01	8.63E-01
J6				9.27E-01

References

1. J. E. P. Connerney, A. Adriani, F. Allegrini, F. Bagenal, S. J. Bolton, B. Bonfond, S. W. H. Cowley, J.-C. Gerard, G. R. Gladstone, D. Grodent, G. Hospodarsky, J. L. Jorgensen, W. S. Kurth, S. M. Levin, B. Mauk, D. J. McComas, A. Mura, C. Paranicas, E. J. Smith, R. M. Thorne, P. Valek, J. Waite, Jupiter's magnetosphere and aurorae observed by the Juno spacecraft during its first polar orbits. *Science* **356**, 826 (2017).

2. C. J. Hansen, M. A. Caplinger, A. Ingersoll, M. A. Ravine, E. Jensen, S. Bolton, G. Orton, Junocam: Juno's outreach camera. *Space Sci. Rev.* 10.1007/s11214-014-0079-x (2014). doi:10.1007/s11214-014-0079-x

3. T. Gehrels, in *Jupiter: Studies of the Interior, Atmosphere, Magnetosphere and Satellites*, T. Gehrels, Ed. (Univ. of Arizona Press, 1976), pp. 531–563.

4. E. García-Melendo, A. Sanchez-Lavega, A study of the stability of jovian zonal winds from HST images: 1995–2000. *Icarus* **152**, 316–330 (2001). doi:10.1006/icar.2001.6646

5. X. S. Asay-Davis, P. S. Marcus, M. H. Wong, I. de Pater, Changes in Jupiter's zonal velocity between 1979 and 2008. *Icarus* **211**, 1215–1232 (2011). doi:10.1016/j.icarus.2010.11.018

6. A. P. Ingersoll, R. F. Beebe, S. A. Collins, G. E. Hunt, J. L. Mitchell, P. Muller, B. A. Smith, R. J. Terrile, Zonal velocity and texture in the jovian atmosphere inferred from Voyager images. *Nature* **280**, 773–775 (1979). doi:10.1038/280773a0

7. D. A. Godfrey, A hexagonal feature around Saturn's north pole. *Icarus* **76**, 335–356 (1988). doi:10.1016/0019-1035(88)90075-9

8. N. Barrado-Izagirre, S. Perez-Hoyos, A. Sanchez-Lavega, Brightness power spectral distribution and waves in Jupiter's upper cloud and hazes. *Icarus* **202**, 181–196 (2009). doi:10.1016/j.icarus.2009.02.015

9. A. Antuñano, T. del Río-Gaztelurrutia, A. Sánchez-Lavega, R. Hueso, Dynamics of Saturn's polar regions. *J. Geophys. Res.* **120**, 155–176 (2015). doi:10.1002/2014JE004709

10. U. A. Dyudina, A. P. Ingersoll, S. P. Ewald, A. R. Vasavada, R. A. West, K. H. Baines, T. W. Momary, A. D. Del Genio, J. M. Barbara, C. C. Porco, R. K. Achterberg, F. M. Flasar, A. A. Simon-Miller, L. N. Fletcher, Saturn's south polar vortex compared to other large vortices in the Solar System. *Icarus* **202**, 240–248 (2009). doi:10.1016/j.icarus.2009.02.014

11. M. A. Janssen, M. Hofstadter, S. Gulkis, A. Ingersoll, M. Allison, S. Bolton, S. Levin, L. Kamp, Microwave remote sensing of Jupiter's atmosphere from an orbiting spacecraft. *Icarus* **173**, 447–453 (2005). doi:10.1016/j.icarus.2004.08.012

12. M. A. Janssen, J. E. Oswald, S. T. Brown, S. Gulkis, S. M. Levin, S. J. Bolton, M. D. Allison, S. K. Atreya, D. Gautier, A. P. Ingersoll, J. I. Lunine, G. S. Orton, T. C. Owen, P. G. Steffes, V. Adumitroaie, A. Bellotti, L. A. Jewell, C. Li, L. Li, S. Misra, F. A.

Oyafuso, D. Santos-Costaz, E. Sarkissian, R. Williamson, J. K. Arballo, A. Kitiyakaral, A. Ulloa-Severino, J. C. Chen, F. W. Maiwald, A. S. Sahakian, P. J. Pingree, K. A. Lee, A. S. Mazer, R. Redick, R. E. Hodges, R. C. Hughes, G. Bedrosian, D. E. Dawson, W. A. Hatch, D. S. Russell, N. F. Chamberlain, M. S. Zawadskil, B. Khayatianl, B. R. Franklin, H. A. Conley, J. G. Kempenaar, M. S. Lool, E. T. Sunada, V. Vorperion, C. C. Wang, MWR: Microwave radiometer for the Juno mission to Jupiter. *Space Sci. Rev.* 10.1007/s11214-017-0349-5 (2017). doi:10.1007/s11214-017-0349-5

13. W. M. Folkner, R. Woo, S. Nandi, Ammonia abundance in Jupiter's atmosphere derived from the attenuation of the Galileo probe's radio signal. *J. Geophys. Res.* **103**, 22847–22855 (1998). doi:10.1029/98JE01635

14. M. H. Wong, P. R. Mahaffy, S. K. Atreya, H. B. Niemann, T. C. Owen, Updated Galileo probe mass spectrometer measurements of carbon, oxygen, nitrogen, and sulfur on Jupiter. *Icarus* **171**, 153–170 (2004). doi:10.1016/j.icarus.2004.04.010

15. M. A. Janssen, Ed., *Atmospheric Remote Sensing by Microwave Radiometry* (Wiley, 1993).

16. P. G. Steffes, T. R. Hanley, B. M. Karpowicz, K. Devaraj, S. Noorizadeh, D. Duong, G. Chinsomboon, A. Bellotti, Michael A. Janssen, S. J. Bolton, high-precision laboratory measurements supporting retrieval of water vapor, gaseous ammonia, and aqueous ammonia clouds with the Juno Microwave Radiometer (MWR). *Space Sci. Rev.* 10.1007/s11214-01600265-0 (2017). doi:10.1007/s11214-01600265-0

17. C. Li, A. Ingersoll, M. Janssen, S. Levin, S. Bolton, V. Adumitroaie, M. Allison, J. Arballo, A. Bellotti, S. Brown, S. Ewald, L. Jewell, S. Misra, G. Orton, F. Oyafuso, P. Steffes, R. Williamson, The distribution of ammonia on Jupiter from a preliminary inversion of Juno Microwave Radiometer data. *Geophys. Res. Lett.* 10.1002/2017GL073159 (2017). doi:10.1002/2017GL073159

18. S. K. Atreya, A. S. Wong, K. H. Baines, M. H. Wong, T. C. Owen, Jupiter's ammonia clouds—localized or ubiquitous? *Planet. Space Sci.* **53**, 498–507 (2005). doi:10.1016/j.pss.2004.04.002

19. A. Adriani, G. Filacchione, T. Di Iorio, D. Turrini, R. Noschese, A. Cicchetti, D. Grassi, A. Mura, G. Sindoni, M. Zambelli, G. Piccioni, M. T. Capria, F. Tosi, R. Orosei, B. M. Dinelli, M. L. Moriconi, E. Roncon, J. I. Lunine, H. N. Becker, A. Bini, A. Barbis, L. Calamai, C. Pasqui, S. Nencioni, M. Rossi, M. Lastri, R. Formaro, A. Olivieri, JIRAM, the Jovian Infrared Auroral Mapper. *Space Sci. Rev.* 10.1007/s11214-014-0094-y (2014). doi:10.1007/s11214-014-0094-y

20. B. A. Archinal, M. F. A'Hearn, E. Bowell, A. Conrad, G. J. Consolmagno, R. Courtin, T. Fukushima, D. Hestroffer, J. L. Hilton, G. A. Krasinsky, G. Neumann, J. Oberst, P. K. Seidelmann, P. Stooke, D. J. Tholen, P. C. Thomas, I. P. Williams, Report of the IAU

Working Group on Cartographic Coordinates and Rotational Elements: 2009. *Celestial Mech. Dyn. Astron.* **109**, 101–135 (2010). doi:10.1007/s10569-010-9320-4

21. G. Sindoni, D. Grassi, A. Adriani, A. Mura, M. L. Moriconi, B. M. Dinelli, G. Filacchione, F. Tosi, G. Piccioni, A. Migliorini, F. Altieri, F. Fabiano, D. Turrini, R. Noschese, A. Cicchetti, S. Stefani, S. J. Bolton, J. E. P. Connerney, S. K. Atreya, F. Bagenal, C. Hansen, A. Ingersoll, M. Jansen, S. M. Levin, J. I. Lunine, G. Orton, M. Amoroso, Characterization of the white ovals on Jupiter's southern hemisphere using the first data by Juno/JIRAM instrument. *Geophys. Res. Lett.* 10.1002/2017GL072940 (2017). doi:10.1002/2017GL072940

22. D. Grassi, A. Adriani, A. Mura, B. M. Dinelli, G. Sindoni, D. Turrini, G. Filacchione, A. Migliorini, M. L. Moriconi, F. Tosi, R. Noschese, A. Cicchetti, F. Altieri, F. Fabiano, G. Piccioni, S. Stefani, S. Atreya, J. Lunine, G. Orton, A. Ingersoll, S. Bolton, S. Levin, J. Connerney, Preliminary results on the composition of Jupiter's troposphere in Hot Spot regions from the JIRAM/Juno instrument. *Geophys. Res. Lett.* 10.1002/2017GL072841 (2017). doi:10.1002/2017GL072841

23. M. Roos-Serote, S. K. Atreya, M. K. Wong, P. Drossart, On the water abundance in the atmosphere of Jupiter. *Planet. Space Sci.* **52**, 397–414 (2004). doi:10.1016/j.pss.2003.06.007

24. R. Jacobson, R. Haw, T. McElrath, P. Antreasian, A comprehensive orbit reconstruction for the Galileo Prime mission in the J2000 system. *Adv. Astronaut. Sci.* **103**, 465–486 (1999).

25. M. Parisi, E. Galanti, S. Finocchiaro, L. Iess, Y. Kaspi, Probing the depth of Jupiter's Great Red Spot with the Juno gravity experiment. *Icarus* **267**, 232–242 (2016). doi:10.1016/j.icarus.2015.12.011

26. J. K. Campbell, S. P. Synnott, Gravity field of the jovian system from Pioneer and Voyager tracking data. *Astrophys. J.* **90**, 364–372 (1985).

27. The JUP230 solution corresponds to the gravity field of Jupiter calculated by R. A. Jacobson in 2003 using Pioneer, Voyager, and Galileo data as released on http://ssd.jpl.nasa.gov/?gravity_fields_op

28. The JUP310 solution corresponds to the gravity field of Jupiter calculated by R. A. Jacobson in 2013 using Pioneer, Voyager, Galileo, and New Horizons data as released on http://ssd.jpl.nasa.gov/?gravity_fields_op

29. N. Nettelmann, A. Becker, B. Holst, R. Redmer, Jupiter models with improved ab initio hydrogen equation of state (H-REOS.2). *Astrophys. J.* **750**, 52 (2012). doi:10.1088/0004-637X/750/1/52

30. Y. Kaspi, T. Guillot, E. Galanti, Y. Miguel, R. Helled, W. Hubbard, B. Militzer, S. Wahl, S. Levin, J. Connerney, S. Bolton, The effect of differential rotation on Jupiter's low-degree

even gravity moments. *Geophys. Res. Lett.* 10.1002/2017GL073629 (2017). doi:10.1002/2017GL073629

31. S. M. Wahl, W. B. Hubbard, B. Militzer, T. Guillot, Y. Miguel, Y. Kaspi, R. Helled, D. D. Reese, N. Movshovitz, E. Galanti, S. Levin, J. Connerney, S. Bolton, Gravity measurements and the role of a dilute core. *Geophys. Res. Lett.* 10.1002/2017GL073160 (2017). doi:10.1002/2017GL073160

32. J. E. P. Connerney, M. Benn, J. B. Bjarno, T. Denver, J. Espley, J. L. Jorgensen, P. S. Jorgensen, P. Lawton, A. Malinnikova, J. M. Merayo, S. Murphy, J. Odom, R. Oliversen, R. Schnurr, D. Sheppard, E. J. Smith, The Juno magnetic field investigation. *Space Sci. Rev.* 10.1007/s11214-017-0334-z (2017). doi:10.1007/s11214-017-0334-z

33. J. E. P. Connerney, M. H. Açuna, N. F. Ness, T. Satoh, New models of Jupiter's magnetic field constrained by the Io Flux Tube footprint. *J. Geophys. Res.* **103**, 11929–11939 (1998). doi:10.1029/97JA03726

34. J. E. P. Connerney, Planetary magnetism. In *Treatise on Geophysics, Volume 10: Planets and Satellites*, G. Schubert, T. Spohn, Eds. (Elsevier, 2015), pp. 195–237; https://ntrs.nasa.gov/archive/nasa/casi.ntrs.nasa.gov/20150011017.pdf.

35. R. Smoluchowski, Jupiter's molecular hydrogen layer and the magnetic field. *Astrophys. J.* **200**, L119–L121 (1975). doi:10.1086/181911

36. W. J. Nellis, S. T. Weir, A. C. Mitchell, Metallization and electrical conductivity of hydrogen in Jupiter. *Science* **273**, 936–938 (1996). doi:10.1126/science.273.5277.936 Medline

37. M. French, A. Becker, W. Lorenzen, N. Nettelmann, M. Bethkenhagen, J. Wicht, R. Redmer, Ab initio simulations for material properties along the Jupiter adiabat. *Astrophys. J. Suppl. Ser.* **202**, 5 (2012). doi:10.1088/0067-0049/202/1/5

38. T. Guillot, D. J. Stevenson, W. B. Hubbard, D. Saumon, in *Jupiter*, F. Bagenal, T. Dowling, W. B. McKinnon, Eds. (Cambridge Univ. Press, 2004), chap. 3.

39. W. B. Hubbard, B. Militzer, A preliminary Jupiter model. *Astrophys. J.* **820**, 80 (2016). doi:10.3847/0004-637X/820/1/80

40. Y. Miguel, T. Guillot, L. Fayon, Jupiter internal structure: The effect of different equations of state. *Astron. Astrophys.* **596**, A114 (2016). doi:10.1051/0004-6361/201629732

41. T. R. Hanley, P. G. Steffes, B. M. Karpowicz, A new model of the hydrogen and helium-broadened microwave opacity of ammonia based on extensive laboratory measurements. *Icarus* **202**, 316–335 (2009). doi:10.1016/j.icarus.2009.02.002

42. K. Devaraj, P. G. Steffes, D. Duong, The centimeter-wavelength opacity of ammonia under deep jovian conditions. *Icarus* **241**, 165–179 (2014). doi:10.1016/j.icarus.2014.06.017

43. A. Bellotti, P. G. Steffes, G. Chinsomboom, Laboratory measurements of the 5-20 cm wavelength opacity of ammonia, water vapor and methane under simulated conditions for

the deep jovian atmosphere. *Icarus* **280**, 255–267 (2016). doi:10.1016/j.icarus.2016.07.013

44. E. C. Morris, R. W. Parsons, Microwave absorption by gas mixtures at pressures up to several hundred bars. I. Experimental technique and results. *Aust. J. Phys.* **23**, 335–349 (1971).

45. V. R. Eshleman, G. L. Tyler, G. E. Wood, G. F. Lindal, J. D. Anderson, G. S. Levy, T. A. Croft, Radio science with Voyager at Jupiter: Initial Voyager 2 results and a Voyager 1 measure of the Io torus. *Science* **206**, 959–962 (1979). doi:10.1126/science.206.4421.959 Medline

46. M. K. Bird, S. W. Asmar, J. P. Brenkle, P. Edenhofer, O. Funke, M. Pätzold, H. Volland, Ulysses radio occultation observations of the Io plasma torus during the Jupiter encounter. *Science* **257**, 1531–1535 (1992). doi:10.1126/science.257.5076.1531 Medline

47. S. W. Asmar, J. W. Armstrong, L. Iess, P. Tortora, Spacecraft Doppler tracking: Noise budget and accuracy achievable in precision radio science observations. *Radio Sci.* **40**, n/a (2005). doi:10.1029/2004RS003101

48. J. A. Barnes, A. R. Chi, L. S. Cutler, D. J. Healey, D. B. Leeson, T. E. McGunigal, J. A. Mullen, W. L. Smith, R. L. Sydnor, R. F. C. Vessot, G. M. R. Winkler, Characterization of frequency stability. *IEEE Trans. Instrum. Meas.* **IM-20**, 105–120 (1971). doi:10.1109/TIM.1971.5570702

49. W. M. Kaula, *Theory of Satellite Geodesy: Applications of Satellites to Geodesy* (Blaisdell, Waltham, MA, 1966).

50. G. Bierman, *Factorization Methods for Discrete Sequential Estimation* (Academic Press, 1997).

51. A. Milani, G. Gronchi, *Theory of Orbit Determination* (Cambridge Univ. Press, 2010).

52. S. V. Gavrilov, V. N. Zharkov, Love numbers of the giant planets. *Icarus* **32**, 443–449 (1977). doi:10.1016/0019-1035(77)90015-X

53. M. Parisi, E. Galanti, S. Finocchiaro, L. Iess, Y. Kaspi, Probing the depth of Jupiter's Great Red Spot with the Juno gravity experiment. *Icarus* **267**, 232–242 (2016). doi:10.1016/j.icarus.2015.12.011

54. D. H. Atkinson, J. B. Pollack, A. Seiff, The Galileo Probe Doppler Wind Experiment: Measurement of the deep zonal winds on Jupiter. *J. Geophys. Res.* **103**, 22911–22928 (1998).

55. D. Grassi, A. Adriani, M. L. Moriconi, N. I. Ignatiev, E. D'Aversa, F. Colosimo, A. Negrão, L. Brower, B. M. Dinelli, A. Coradini, G. Piccioni, Jupiter's hot spots: Quantitative assessment of the retrieval capabilities of future IR spectro-imagers. *Planet. Space Sci.* **58**, 1265–1278 (2010). doi:10.1016/j.pss.2010.05.003

56. C. R. Rodgers, *Inverse Methods for Atmospheric Sounding: Theory and Practice* (World Scientific, 2000).

57. P. G. J. Irwin, N. A. Teanby, R. de Kok, L. N. Fletcher, C. J. A. Howett, C. C. C. Tsang, C. F. Wilson, S. B. Calcutt, C. A. Nixon, P. D. Parrish, The NEMESIS planetary atmosphere radiative transfer and retrieval tool. *J. Quant. Spectrosc. Radiat. Transf.* **109**, 1136–1150 (2008). doi:10.1016/j.jqsrt.2007.11.006

58. A. Kylling, K. Stamnes, S.-C. Tsay, A reliable and efficient two-stream algorithm for spherical radiative transfer: Documentation of accuracy in realistic layered media. *J. Atmos. Chem.* **21**, 115–150 (1995). doi:10.1007/BF00696577

59. A. P. Showman, T. E. Dowling, Nonlinear simulations of Jupiter's 5-micron hot spots. *Science* **289**, 1737–1740 (2000). 10.1126/science.289.5485.1737 Medline

60. R. Hueso, A. Sánchez-Lavega, Motions in hot spot-plume regions using Voyager images. *Icarus* **136**, 353–357 (1998). doi:10.1006/icar.1998.6018

61. D. Choi, A. P. Showman, A. R. Vasavada, A. A. Simon-Miller, Meteorology of Jupiter's equatorial hot spot and plumes from Cassini. *Icarus* **223**, 832–843 (2013). doi:10.1016/j.icarus.2013.02.001